The Astrophysical Journal, 960:96 (15pp), 2024 January 10 https://doi.org/10.3847/1538-4357/ad05cd

The Atacama Cosmology Telescope: Galactic Dust Structure and the Cosmic PAH Background in Cross-correlation with WISE

Rodrigo Córdova Rosado[1], Brandon S. Hensley[1], Susan E. Clark[2,3], Adriaan J. Duivenvoorden[4], Zachary Atkins[5], Elia Stefano Battistelli[6], Steve K. Choi[7,8], Jo Dunkley[1,5], Carlos Hervías-Caimapo[9], Zack Li[10], Thibaut Louis[11], Sigurd Naess[12], Lyman A. Page[5], Bruce Partridge[13], Cristóbal Sifón[14], Suzanne T. Staggs[5], Cristian Vargas[9], and Edward J. Wollack[15]

[1] Department of Astrophysical Sciences, Peyton Hall, Princeton University, 4 Ivy Lane, Princeton, NJ 08544, USA
[2] Department of Physics, Stanford University, Stanford, CA 94305, USA
[3] Kavli Institute for Particle Astrophysics & Cosmology, Stanford University, P.O. Box 2450, Stanford, CA 94305, USA
[4] Center for Computational Astrophysics, Flatiron Institute, 162 5th Avenue, New York, NY 10010, USA
[5] Joseph Henry Laboratories of Physics, Jadwin Hall, Princeton University, Princeton, NJ 08544, USA
[6] Sapienza University of Rome, Physics Department, Piazzale Aldo Moro 5, I-00185 Rome, Italy
[7] Department of Physics, Cornell University, Ithaca, NY 14853, USA
[8] Department of Astronomy, Cornell University, Ithaca, NY 14853, USA
[9] Instituto de Astrofísica and Centro de Astro-Ingeniería, Facultad de Física, Pontificia Universidad Católica de Chile, Av. Vicuña Mackenna 4860, 7820436 Macul, Santiago, Chile
[10] Canadian Institute for Theoretical Astrophysics, University of Toronto, Toronto, ON M5S 3H8, Canada
[11] Université Paris-Saclay, CNRS/IN2P3, IJCLab, F-91405 Orsay, France
[12] Institute of Theoretical Astrophysics, University of Oslo, Norway
[13] Department of Physics and Astronomy, Haverford College, Haverford, PA 19041, USA
[14] Instituto de Física, Pontificia Universidad Católica de Valparaíso, Casilla 4059, Valparaíso, Chile
[15] NASA/Goddard Space Flight Center, Greenbelt, MD 20771, USA
Received 2023 July 12; revised 2023 October 20; accepted 2023 October 21; published 2024 January 2

Abstract

We present a cross-correlation analysis between 1′ resolution total intensity and polarization observations from the Atacama Cosmology Telescope (ACT) at 150 and 220 GHz and 15″ mid-infrared photometry from the Wide-field Infrared Survey Explorer (WISE) over 107 $12.^{\circ}5 \times 12.^{\circ}5$ patches of sky. We detect a spatially isotropic signal in the WISE×ACT *TT* cross-power spectrum at 30σ significance that we interpret as the correlation between the cosmic infrared background at ACT frequencies and polycyclic aromatic hydrocarbon (PAH) emission from galaxies in WISE, i.e., the cosmic PAH background. Within the Milky Way, the Galactic dust *TT* spectra are generally well described by power laws in ℓ over the range $10^3 < \ell < 10^4$, but there is evidence both for variability in the power-law index and for non-power-law behavior in some regions. We measure a positive correlation between WISE total intensity and ACT *E*-mode polarization at $1000 < \ell \lesssim 6000$ at $>3\sigma$ in each of 35 distinct $\sim$100 deg^2 regions of the sky, suggesting that alignment between Galactic density structures and the local magnetic field persists to subparsec physical scales in these regions. The distribution of *TE* amplitudes in this ℓ range across all 107 regions is biased to positive values, while there is no evidence for such a bias in the *TB* spectra. This work constitutes the highest-ℓ measurements of the Galactic dust *TE* spectrum to date and indicates that cross-correlation with high-resolution mid-infrared measurements of dust emission is a promising tool for constraining the spatial statistics of dust emission at millimeter wavelengths.

Unified Astronomy Thesaurus concepts: Interstellar dust (836); Dust continuum emission (412); Interstellar magnetic fields (845); Cosmic background radiation (317); Interstellar medium (847); Polycyclic aromatic hydrocarbons (1280)

1. Introduction

The interstellar medium (ISM) is a turbulent environment. Energy is injected at large physical scales by processes like stellar feedback, and a complex turbulent energy cascade shapes the ISM over a vast range of physical scales (e.g., Ferrière 2001; Elmegreen & Scalo 2004). High dynamic range observations of interstellar emission are critical for understanding the flow of mass and energy in the ISM (e.g., Fissel et al. 2019a; Stinebring et al. 2019). One common approach is to measure the power spectrum of ISM emission using tracers like neutral hydrogen (H I) emission or interstellar dust. These power spectra are often found to be well described by a power law, with a power spectral index that can be compared to theoretical predictions (e.g., Crovisier & Dickey 1983; Miville-Deschênes et al. 2003a; Miville-Deschênes & Lagache 2005; Miville-Deschênes et al. 2007; Martin et al. 2010, 2015; Blagrave et al. 2017; Pingel et al. 2022).

Combining observations of dust emission from Planck and the Wide-field Infrared Survey Explorer (WISE; Wright et al. 2010) with MegaCam measurements of optical scattering from dust, Miville-Deschênes et al. (2016) demonstrated that the dust power spectrum in total intensity (i.e., *TT*) is well fit by a power law $k^{-2.9\pm0.1}$ from scales of degrees to $\sim 1''$, corresponding to physical scales of $\sim$0.01 pc. The power spectral index of the observable column density is related to the statistics of the 3D density field, which are in turn affected by turbulence and the phase distribution of the gas, but are not directly measurable due to projection effects (Miville-Deschênes et al. 2003b; Clark et al. 2019; Kalberla & Haud 2019; Marchal &

Miville-Deschênes 2021). On scales greater than 5′, this index is consistent with measurements across the sky from the Planck satellite (Planck Collaboration XXX 2014; Planck Collaboration Int. XLVIII 2016). In this work, we investigate the variability of this power-law index at smaller scales ($10^3 < \ell < 10^4$, corresponding to $10' > \theta > 1'$).

Planck observations established a robust positive correlation between dust total intensity and dust *E*-mode polarization (i.e., *TE*) for multipoles $\ell \lesssim 600$ over much of the sky (Planck Collaboration XI 2020). Such a correlation is expected if dust-bearing ISM structures are elongated along magnetic field lines (Zaldarriaga 2001; Huffenberger et al. 2020; Clark et al. 2021). Indeed, H I filaments are ubiquitous across the sky with orientations that are strongly correlated with the measured dust polarization angles (Clark et al. 2015; Clark & Hensley 2019). H I structure can thus be used to measure properties of Galactic dust polarization in cross-correlation (BICEP/Keck Collaboration et al. 2023; Halal et al. 2023). Filament-based models successfully reproduce the observed *TE* correlation (Hervías-Caimapo & Huffenberger 2022). However, in dense regions, it is observed that ISM structures are preferentially oriented perpendicular to magnetic field lines (i.e., negative *TE*; Planck Collaboration Int. XXXV 2016; Bracco et al. 2019). In this work, we extend the characterization of the *TE* correlation to smaller scales ($1000 < \ell \lesssim 6000$).

To probe the small-scale *TT* and *TE* spectra of Galactic dust emission, we employ new maps of millimeter dust emission from the Atacama Cosmology Telescope (ACT) in both total and polarized intensity. The combination of sensitivity, angular resolution, and sky coverage (sky fraction $f_{\rm sky} \simeq 40\%$) afforded by ACT observations enables characterization of dust at arcminute scales over a large sky area and thus our investigation of the universality of the small-scale dust power spectrum across a range of Galactic environments. We employ ACT maps from two broad bands centered roughly at 150 and 220 GHz with angular resolutions of 1.′4 and 1.′0, respectively.

We complement the ACT data with full-sky observations of mid-infrared (MIR) emission from WISE. In particular, we use the maps of diffuse emission extracted from observations in the W3 passband by Meisner & Finkbeiner (2014; hereafter MF14). Their custom processing of the WISE data removes compact sources and associated data artifacts. The resulting map covers the full sky at 15″ resolution with noise properties independent of ACT, enabling correlation analysis down to the ACT resolution limit.

The broad W3 passband is centered at 12 μm but has an appreciable spectral response from ≃8 to 16 μm (Wright et al. 2010). For regions typical of the diffuse ISM of the Galaxy, emission at these wavelengths is dominated by the 7.7, 11.3, and 12.7 μm MIR emission features associated with polycyclic aromatic hydrocarbons (PAHs; e.g., Tielens 2008). Continuum emission is also present from PAHs and likely other nanoparticles undergoing single-photon heating. Other expected sources of diffuse emission in this map include the zodiacal light and the extragalactic background light.

As a ubiquitous component of the Galactic dust population, PAHs are generally well coupled to the larger grains responsible for far-infrared and millimeter emission (e.g., Mattila et al. 1996; Onaka et al. 1996; Draine & Li 2007). Empirically, strong correlations have been observed between the MF14 map and dust emission in the Planck bands (Hensley et al. 2016). However, the mass fraction of dust in the form of PAHs varies over the sky (Hensley et al. 2016; Planck Collaboration Int. XXIX 2016) with an apparent dependence on ISM phase (Hensley et al. 2022). Further, the PAH emission spectrum is sensitive to the intensity and spectrum of the interstellar radiation field (Draine et al. 2021). Thus, PAH emission and millimeter dust emission will not be perfectly correlated in detail.

In this work, we assess the ability of high-resolution observations of MIR dust emission to correlate with—and thus predict—dust emission properties at millimeter wavelengths. We then use this combination of independent data sets to characterize the Galactic dust power spectrum at small scales in both intensity and polarization, as well as its variation across the sky.

The MF14 WISE W3 map isolates all diffuse emission falling into the W3 passband. In principle, this includes emission from unresolved galaxies across cosmic time. Chiang & Ménard (2019) found that the MF14 map has a statistically significant correlation with optical measurements of galaxies and active galactic nuclei from redshifts $z \lesssim 2$. They interpreted this as redshifted PAH emission from galaxies, i.e., the cosmic PAH background. Indeed, the 7.7 μm PAH feature is the strongest of the PAH features and remains in the W3 passband until $z \sim 1$. In this work, we find robust evidence for a spatially isotropic correlation between the MF14 WISE W3 map and ACT maps at both 150 and 220 GHz that we interpret as the first detection of the cosmic PAH background in cross-correlation with the cosmic infrared background (CIB).

This paper is organized as follows. In Section 2, we summarize the data products used in this analysis. In Section 3, we outline our methodologies for power spectrum computation, uncertainty quantification, and parameter estimation. We present the results of our total intensity × total intensity (*TT*) analysis and our total intensity × *E*-mode polarization (*TE*) analysis in Sections 4 and 5, respectively. In Section 6, we discuss the implications of our results on both the structure of the ISM and the cosmic PAH background, and we conclude in Section 7.

2. Data

2.1. ACT

ACT has measured the total intensity and linear polarization of the millimeter sky over 18,000 deg^2. ACT observed in five passbands: f030 (22–32 GHz), f040 (29–48 GHz), f090 (79–112 GHz), f150 (124–171 GHz), and f220 (171–276 GHz). In this paper, we make use of *I*, *Q*, and *U* Stokes maps made from f150 and f220 observations, with angular resolutions of 1.′4 and 1.′0, respectively (Henderson et al. 2016; Thornton et al. 2016; Naess et al. 2020). All of the f150 maps employed in this analysis coadd the three detector arrays that observed in the band; only one array observed in the f220 band.

We use maps made using the f150 and f220 data from the 2008–2019 observing seasons[16] following a similar process used in making the publicly available Data Release 5 (DR5) maps,[17] which only used data taken through 2018 (Naess et al. 2020).

[16] These 2008–2019 maps are not a major data release for ACT, but the DR5 2008–2018 maps are available, and the upcoming DR6 maps from the 2008–2022 data will be made public. We compare the measured W3×ACT f150 and f220 *TT* and *TE* spectra from the 2008–2019 data set used in this analysis to the spectra computed with the publicly available 2008–2018 DR5 data set (Naess et al. 2020) in two regions. Uncertainties on the power spectra decrease by ∼20% with the inclusion of the 2019 data. A model fit yields parameters that change by less than 1σ for both *TT* and *TE* fits between the data sets.

[17] https://lambda.gsfc.nasa.gov/product/act/actpol_prod_table.html

These maps use the same Plate Carrée (CAR) projection as the DR5 maps and have a pixel size of approximately 0′.5. These maps do not include any Planck data directly but have been scaled by an overall multiplicative factor that minimizes the residual relative to the Planck temperature power spectrum in the range $1000 < \ell < 2000$ (Naess et al. 2020). We use maps that include data taken during both night and day and from which point sources detected at greater than 5σ have been subtracted, resulting in a subtraction threshold of ∼15 mJy in the f150 band.

We use the ACT-produced ACT+Planck coadded Q and U maps at f150 and f220 for our polarization analysis to enhance our sensitivity at $\ell \lesssim 2000$. The maps are constructed by combining the coadded ACT f150 and f220 maps described above with the Planck PR2 and PR3 143 and 217 GHz maps (Planck Collaboration I 2016, 2020) using the coadding procedure described in Naess et al. (2020).

The maps have associated products including inverse variance maps, which include a per pixel estimate of the inverse variance in μK^{-2}, as well as beam window functions and passbands. The maps are converted from cosmic microwave background (CMB) temperature units to MJy sr^{-1} using conversion factors of 395 and 482 MJy sr^{-1} K^{-1} for f150 and f220, respectively, derived assuming the approximate ACT band centers for a Rayleigh–Jeans spectrum (150 and 220 GHz, respectively). We consider scales $\ell > 1000$ for the f150 total intensity analysis and all polarization analyses, but only $\ell > 1400$ for the f220 total intensity analysis to avoid scales that are expected to suffer from a loss of power due to modeling errors in the mapmaking process (Naess & Louis 2023). We use the HEALPix/COSMO polarization convention[18] throughout. The overall systematic uncertainties are at the level of 10% (Naess et al. 2020), which includes both map calibration uncertainties and unit conversion errors from use of the ACT band centers rather than full bandpass integration.

2.2. Planck

We use the Planck 353 GHz maps[19] produced with the NPIPE data processing pipeline (Planck Collaboration Int. LVII 2020) to extend our analysis to higher frequencies and provide a point of comparison with the ACT measurements. The Planck 353 GHz channel is the highest Planck frequency designed to measure linear polarization and is the channel most sensitive to polarized thermal dust emission. The maps are provided in units of kelvins, which we convert to MJy sr^{-1} via a conversion factor of 287.5 MJy sr^{-1} K^{-1} (Planck Collaboration III 2020).

2.3. WISE

The WISE satellite observed the full sky in four bands across the MIR (Wright et al. 2010). The WISE W3 band is centered at ∼12 μm and spans the 8.6, 11.3, and 12.7 μm vibrational emission features of PAHs that dominate Galactic cirrus emission at these frequencies (e.g., Mattila et al. 1996; Ingalls et al. 2011).

MF14 produced a map of diffuse Galactic emission from the full-sky W3 data by modeling and subtracting emission from point sources, solar system objects, diffraction spikes, compact sources, and Moon and zodiacal light contamination. MF14 combined the W3 data with Planck 857 GHz (350 μm) data to recover extended emission at scales greater than 2°. The MF14 data are provided as a set of 430 12.°5 × 12.°5 tiles smoothed to an angular resolution of 15″ FWHM. Approximately 200 of the 430 tiles overlap significantly (>50%) with the ACT footprint. We smooth these data to a final resolution of 45″ before reprojecting onto the ACT pixelization and CAR projection using the `pixell`[20] package (Naess et al. 2021).

The WISE tiles are provided as fluxes $F_{\rm W3}$ in units of digital number (DN), which we convert to MJy sr^{-1} following Cutri et al. (2012),

$$I_\nu = \frac{F_{\nu 0}}{\theta_{\rm pix}^2} 10^{-(M_{0,\rm inst}+\Delta m - 8.926)/2.5} \frac{F_{\rm W3}}{\rm DN}$$
$$= 0.0135 \frac{F_{\rm W3}}{\rm DN} \ {\rm MJy\ sr^{-1}} \quad , \tag{1}$$

where $F_{\nu 0} = 31.674$ Jy is the W3 zero-magnitude flux density of a source with $F_\nu \propto \nu^{-2}$ (Jarrett et al. 2011), $\theta_{\rm pix} = 2.''75$ is the W3 pixel size (Mainzer et al. 2005), $M_{0,\rm inst} = 17.800$ is the instrumental zero-point (Cutri et al. 2012), $\Delta m = 5.174$ is the conversion from the WISE Vega system magnitudes to AB magnitudes (Jarrett et al. 2011), and 8.926 is the factor relating the flux density in janskys to AB magnitudes (Tokunaga & Vacca 2005). In detail, the conversion between DN and MJy sr^{-1} depends on the spectrum of the source; Equation (1) is strictly accurate only for spectra with $F_\nu \propto \nu^{-2}$. However, the conversion factor differs by $\lesssim$13% for power-law indices between −3 and 3 (Wright et al. 2010).

3. Methodology

3.1. Power Spectrum Estimation

We compute the angular power spectra in each tile using standard partial-sky pseudo-C_ℓ methods (e.g., Hivon et al. 2002). We compute the *TT*, *TE*, and *TB* cross-spectra between the WISE *I* total intensity map and the ACT *I*, *Q*, and *U* maps using the `nawrapper`[21] interface to the `NaMaster` software (Alonso et al. 2019). The mask is described in Section 3.2. We bin the measurements with $\ell(\ell+1)$ weighting, with equally spaced logarithmic bins from $\ell = 1000$ to 10,000 for f150 and $\ell = 1400$ to 10,000 for f220 (see Section 2.1).

To compute the uncertainty on a binned cross-spectrum C_b^{xy}, where x and y are any of T, E, or B, we start from the analytic expression (Knox 1995; Hivon et al. 2002),

$$\sigma^2(C_b^{xy}) = \frac{(C_b^{xy})^2 + (C_b^{xx} C_b^{yy})}{f_{\rm sky} \frac{w_2^2}{w_4} (2\ell + 1)\Delta\ell} \quad , \tag{2}$$

where $f_{\rm sky}$ is the fractional area of the sky, $\Delta\ell$ is the bin width, and ℓ is the bin midpoint. The correction factor w_2^2/w_4 accounts for the apodization of the mask. The w_i factors are defined as $w_i \equiv \sum \Omega_j W_j^i$, where Ω_j is the pixel area, and W_j is the value of the apodized mask in pixel j (Hivon et al. 2002). The auto-power spectrum term is the sum of a signal and a noise term

[18] https://lambda.gsfc.nasa.gov/product/about/pol_convention.html
[19] https://pla.esac.esa.int/#maps
[20] Available online at www.github.com/simonsobs/pixell
[21] Introduced in Li et al. (2020) and available through GitHub at https://github.com/xzackli/nawrapper.

(i.e., $C_b^{xx} = S_b^{xx} + N_b^{xx}$), while the cross-power spectrum is signal-only (i.e., $C_b^{xy} = S_b^{xy}$).

However, Equation (2) neglects the effects of mode coupling induced by the mask. To account for this, we employ the `NaMaster` implementation of analytic methods to compute the full covariance matrix (García-García et al. 2019). Since calculation of the full covariance matrix for all of the cross-spectra used in our analysis is computationally expensive, we compute it only for the WISE W3×f150 spectrum in each region in *TT*. We then approximate the per-band uncertainties of each of the other spectra (*TT* at f220 and both *TE* and *TB* at f150, f220, and 353 GHz) using the simpler expression in Equation (2) rescaled by the ratio between the uncertainty computed from the diagonal of the full covariance matrix and from Equation (2) at f150. This increases the uncertainties by ∼10%, with some scale dependence. Note that only the diagonal entries of the covariance matrix are used for plotting error bars and in parameter estimation.

We apply the same correction derived from the *TT* spectrum to both the *TE* and *TB* uncertainties. Because the same sky mask is used for all frequencies and for all of *TT*, *TE*, and *TB*, this is a good approximation.

To further ensure the robustness of this approach, we exclude regions from our analysis for which the off-diagonal terms of the covariance matrix are large. Specifically, if including the off-diagonal elements of the covariance matrix changes the χ^2 of our best-fit model (see Section 3.3) by more than 2 for 20 degrees of freedom, then that region is discarded. In practice, this removes regions with particularly complicated masks, e.g., many disconnected regions.

Equation (2) accounts for the contribution of sample variance to the total uncertainty. It would be appropriate to neglect sample variance in reporting the cross-power spectrum of emission in a given region, since the error bars are reflecting only how well the particular spectrum of that region is being measured (see, e.g., the discussion in Planck Collaboration Int. XXX 2016). In contrast, sample variance should be included when fitting a model for the underlying spectrum from which the observed spectrum is drawn. As such, model fitting is a principal focus of our analysis, and we include sample variance in all error bars throughout this work. Sample variance is typically $\lesssim$10% of the total uncertainty at all ℓ.

3.2. Masking

Our primary mask for each region is a circle in R.A. and decl. with a diameter of approximately 11°. We apodize this mask with the `C1` cosine taper implemented in `NaMaster` using an apodization scale of 1°.

The MF14 W3 data include a bitmask of data quality flags. We mask all pixels affected by saturated point sources, the first and second latent points of source ghosts, linelike effects, and Moon and solar system object contamination (corresponding to flags 0, 3, 8, 14, 15, 18, and 20), as well as all pixels without a flux measurement. Point sources brighter than 15 mJy at f150, predominantly active galactic nuclei (AGN; Marsden et al. 2014), are masked with circular holes of radius 5′. We apply an additional mask of 14 extended sources identified in ACT maps to mitigate contamination from objects like planetary nebulae and resolved galaxies. This mask was created for the upcoming ACT DR6 power spectrum analysis by visual inspection of the maps after the initial source mask was applied.

We do not mask pixels flagged by MF14 as "compact resolved sources" (flag 7). These are mostly galaxies, most of which would not be detected in the ACT maps. We do not wish to remove extragalactic signal, particularly in an inhomogeneous way across the sky, as this would complicate our analysis of extragalactic cross-correlations. On the other hand, it is likely that flag 7 also identifies some compact resolved Galactic sources that, if retained, would affect our power spectra, particularly at high ℓ. On balance, we prefer to leave all pixels flagged by flag 7 in our analysis but note that a careful separation of Galactic versus extragalactic compact resolved sources could improve the analysis presented in this work.

We apodize the source and artifact mask at an apodization scale of 18′ using the `C1` cosine taper implemented in `NaMaster`. The 18′ apodization scale follows the nominal choices for the upcoming ACT CMB power spectrum analysis. Our final mask combines the source and artifact mask with the primary circular mask. Each region has a single mask that is used for all analyses at all frequencies.

We select WISE tiles that overlap entirely with the ACT footprint, retain at least 33 deg^2 of sky area after the mask is applied, and pass the covariance matrix criterion described in Section 3.1. This results in 107 regions encompassing 6190 deg^2, or 15% of the sky, after masking. These regions are illustrated in Figure 1 and span roughly 2 orders of magnitude in dust column density.

3.3. Power-law Fitting

We fit simple power-law models to the *TT* and *TE* spectra. Following similar analyses (e.g., Planck Collaboration XI 2020), the Galactic signal at each frequency is modeled as a power law of the form $A_d(\ell/\ell_0)^{\alpha_d}$. We expect $\alpha_d \approx -3$ and for A_d to scale with the dust intensity.

For the *TT* spectra, we also include an extragalactic signal that can arise from the cross-correlation of the CIB seen by both WISE and ACT. We use a three-component model containing the Galactic component, a clustered extragalactic component (CIB-C), and a Poisson-like extragalactic component (CIB-P), with the total power spectrum given by

$$C_\ell^{TT} = A_d\left(\frac{\ell}{1000}\right)^{\alpha_d} + A_C\left(\frac{\ell}{7000}\right)^{\alpha_C} + A_P \quad . \tag{3}$$

Here A_C is the amplitude of the clustered component, and α_C is its power-law index. A_P is the scale-independent amplitude of the Poisson component. We define $A_{\rm CIB} = A_C + A_P$ as a measure of the total extragalactic power at $\ell = 7000$.

We use the Markov Chain Monte Carlo (MCMC) methods implemented in `emcee` (Foreman-Mackey et al. 2013) to estimate parameters using a Gaussian likelihood

$$-2\ln\mathcal{L} = (C_b - w_{b\ell}C_\ell)^T Q^{-1}(C_b - w_{b\ell}C_\ell) \tag{4}$$

up to an additive constant. Here C_ℓ is the model vector, $w_{b\ell}$ are the bandpower window functions that weight the model given the effects of the mode coupling matrix, C_b is the binned data vector, and Q is the diagonal covariance matrix.

We do not expect a significant extragalactic contribution to the *TE* spectra, so we use a simpler two-parameter Galactic model of the form

$$C_\ell^{TE} = A_d\left(\frac{\ell}{1000}\right)^{\alpha_d} \quad . \tag{5}$$

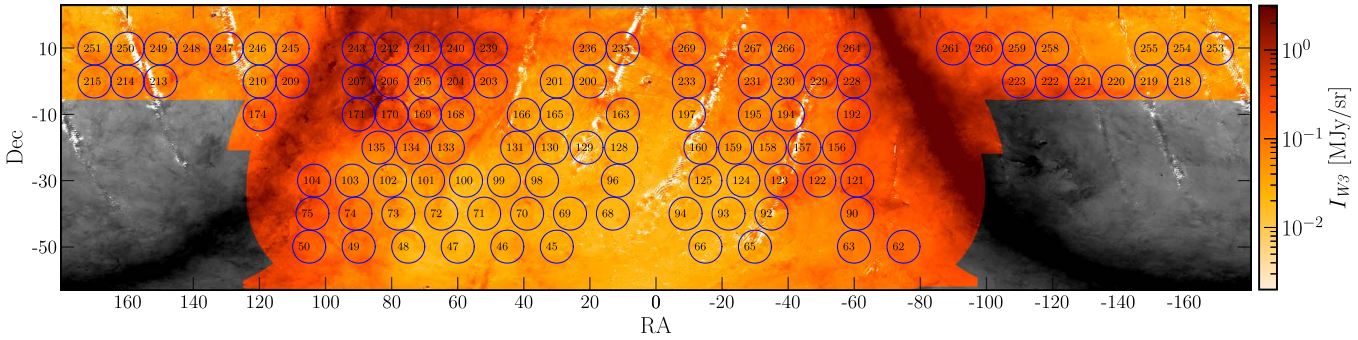

Figure 1. Locations of the 107 MF14 WISE tiles analyzed in this work overlaid on the MF14 W3 diffuse emission map. Each $\sim 11^\circ$ diameter circle represents the analysis mask adopted in the present study. Areas outside the ACT footprint are rendered in gray scale. White regions, such as the prominent Moon contamination features, are pixels masked by MF14.

Since the signal-to-noise ratio of the *TE* spectra is lower than that for *TT*, we fix $\alpha_d = -2.5$ in the baseline analysis following fit values at lower multipoles (Planck Collaboration XI 2020).

4. Total Intensity Analysis

4.1. Power Spectra

We detect a robust correlation between the WISE and ACT maps over nearly the entire region of sky analyzed. Specifically, for 106 of 107 regions in our analysis, we reject the model $C_\ell^{TT} = 0$ at $>3\sigma$ for both W3×f150 and W3×f220. A selection of five W3×f150 *TT* spectra spanning a range of column densities is presented in Figure 2. The highest column density tiles shown have roughly power-law spectra with $C_\ell \propto \ell^{-3}$, as has been seen for Galactic dust emission (e.g., Gautier et al. 1992; Bracco et al. 2011; Hajian et al. 2012; Planck Collaboration XXX 2014). While the lower column density regions of Figure 2 are consistent with this behavior at larger scales ($\ell \lesssim 3000$), all have a rising spectrum in $\mathcal{D}_\ell \equiv \ell(\ell+1)C_\ell/2\pi$ at higher multipoles. Similar behavior is observed with f220 (not shown).

As an initial validation check of the *TT* spectra, we perform a null test by computing the cross-spectra between WISE data in one region with ACT data in different regions of sky. Specifically, for each of a set of four WISE maps, we compute the W3×f150 spectrum with 10 different ACT regions at the same decl. As expected, all *TT* spectra are consistent with zero. For the 40 *TT* spectra consisting of 22 bins each, we find $\chi^2 = 838$ for $C_\ell^{TT} = 0$ versus 880 degrees of freedom (correspondingly, with a probability to exceed (PTE) of 84%).

We therefore seek a physical explanation of the rising *TT* spectrum at high multipoles. In the following section, we demonstrate that this signal is compatible with extragalactic background fluctuations correlated between WISE and ACT frequencies.

4.2. Fitting the Extragalactic Background

Given that a single power law in ℓ is an inadequate description of the *TT* spectra presented in Figure 2, we consider the model described in Equation (3) that includes an extragalactic component. Extragalactic emission should have the same amplitude across the sky, while the Galactic dust emission should vary from region to region. To avoid assuming a constant Galactic dust α_d across all tiles, we proceed in two steps. First, we infer the extragalactic component parameters

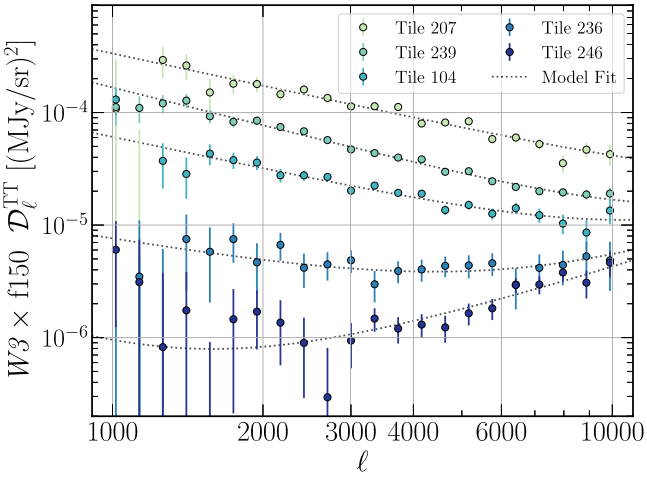

Figure 2. WISE W3×ACT f150 *TT* spectra of selected regions of varying column density. The slopes of the best-fit power laws are consistent with previous measurements of Galactic dust power spectra ($\alpha_d \sim -3$). In lower column density regions, we see evidence of an extragalactic component. The best-fit model for each region is shown with a dotted line.

A_C and A_P from a simultaneous fit to six regions (tiles 70, 133, 159, 166, 246, and 255) of low column density (median $N_{\mathrm{H\,I}} \lesssim 2.5 \times 10^{20}\ \mathrm{cm}^{-2}$). We then hold A_C and A_P fixed to their best-fit values to fit A_d and α_d in each region separately.

To fit Equation (3) to the six selected regions simultaneously, we first fix α_d and α_C to representative values of -3 and -1, respectively (see, e.g., Addison et al. 2012). We then fit the six A_d parameters, one A_C parameter, and one A_P parameter, all with positive definite priors using the methods described in Section 3.3. The A_C and A_P posteriors for the f150 fit are presented in Figure 3 with best-fit values from both the f150 and f220 fits listed in Table 1. We have verified that a simple joint Gaussian likelihood fit to all 107 tiles simultaneously with $\alpha_d = -3$ and $\alpha_C = -1$ yields consistent best-fit values of A_C and A_P.

We find that $A_{\mathrm{CIB}} = A_C + A_P > 0$ at 30σ significance at both f150 ($A_{\mathrm{CIB}} = 3.4 \pm 0.1 \times 10^{-13}\ (\mathrm{MJy\ sr^{-1}})^2$) and f220 ($A_{\mathrm{CIB}} = 1.44 \pm 0.05 \times 10^{-12}\ (\mathrm{MJy\ sr^{-1}})^2$). The fits yield a ratio $\mathcal{F}_{\mathrm{iso}} \equiv A_{\mathrm{CIB}}^{\mathrm{f220}}/A_{\mathrm{CIB}}^{\mathrm{f150}} = 4.2 \pm 0.2$. The systematic uncertainty on these numbers is of order 10% (see Section 2.1). Dunkley et al. (2013) performed multifrequency fits to the CIB signal in ACT f150 and f220 using a modified blackbody model $I_\nu \propto \nu^\beta B_\nu(T_d)$ for the frequency dependence, where $B_\nu(T)$ is the Planck function, and T_d is the dust temperature.

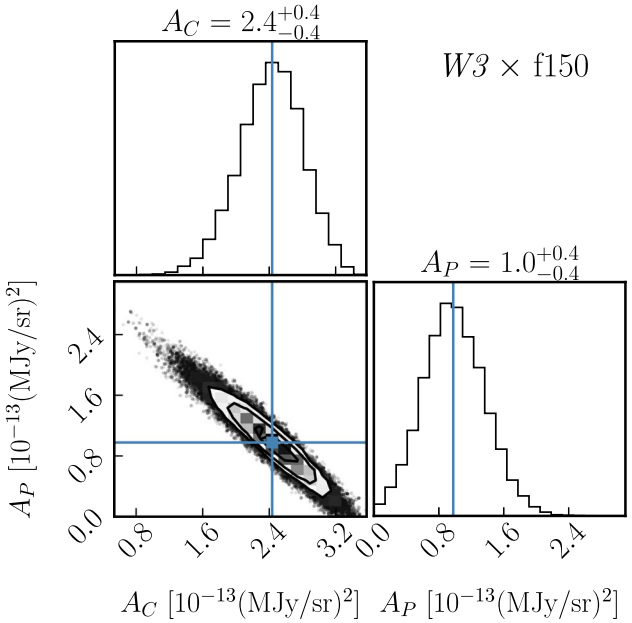

Figure 3. Posteriors for the clustered (A_C) and Poisson (A_P) components of the fit to the isotropic high-ℓ signal in f150 over six low column density regions. We marginalize over the Galactic dust emission in each region by fitting a Galactic dust amplitude (A_d) in each region assuming $\alpha_d = -3$. A nonzero signal ($A_C + A_P$) is detected at 30σ significance.

Table 1
Isotropic Background Parameters

	W3×f150 [10^{-12} (MJy sr^{-1})^2]	W3×f220 [10^{-12} (MJy sr^{-1})^2]
A_C	0.24 ± 0.04	1.2 ± 0.2
A_P	0.10 ± 0.04	0.2 ± 0.2
$A_{\rm CIB}$	0.34 ± 0.01	1.44 ± 0.05

Note. Extragalactic background parameters estimated from WISE×ACT *TT* spectra in six regions of low dust column density. A fixed $\alpha_d = -3$ and $\alpha_C = -1$ were assumed (see Equation (3)).

They found $\beta = 2.2 \pm 0.1$ for a fixed dust temperature $T_d = 9.7$ K, equivalent to $\mathcal{F}_{\rm iso} = 4.1 \pm 0.2$. Thus, our derived value is consistent with previous ACT measurements of the CIB at millimeter wavelengths. We have likewise verified that the fitted Galactic dust A_d parameters at f150 and f220 are consistent with a typical frequency scaling for Galactic dust emission, although, by design, the Galactic dust signal is weak in these regions, and the constraints are not stringent.

The amplitudes A_C and A_P are strongly anticorrelated, and the Poisson component is not measured at high significance. To investigate this further, we perform a fit with just one extragalactic component where we fit for both amplitude and slope. For the latter, we impose a uniform prior $[-2, 1]$. This fit excludes $\alpha = 0$ at $>5\sigma$; i.e., a pure Poisson component is strongly disfavored. On the other hand, if we fix $\alpha_C = -1$ and $A_P = 0$, we find little degradation in the goodness of fit (PTE = 0.42 versus 0.51 for the fiducial model). In another variation, we fit A_P, A_C, and α_C, imposing a uniform prior on α_C of $[-1.5, -0.5]$. We find that $\alpha_C \leqslant -0.76$ at 95% confidence. The data therefore require a component that resembles the clustered component of the CIB but do not require a Poisson component. However, given the extent of the degeneracy between A_C and A_P (see Figure 3), we cannot place strong constraints on their relative amplitudes.

We have found a high-ℓ *TT* correlation between the WISE and ACT maps that is well fit with a single amplitude across six regions and with amplitudes at f150 and f220 consistent with the frequency scaling of the CIB. We therefore interpret this signal as a correlation between galaxies observed by both WISE and ACT. Possible origins of the extragalactic component are discussed further in Section 6.4, but we will first verify that this component is indeed of constant amplitude across the remaining 101 regions.

For all subsequent *TT* fits, we fix the A_C and A_P parameters to their fit values at a given frequency (see Table 1) and fix $\alpha_C = -1$.

4.3. Fitting the Galactic Dust TT Spectrum

4.3.1. Goodness of Fit

In the previous section, we derived the best-fit values of the extragalactic parameters in our *TT* model (A_C and A_P in Equation (3)) based on a set of six regions. In this section, we fix A_C and A_P to these values (see Table 1) and perform another MCMC fit separately in each of the 107 regions to derive A_d and α_d. In these fits, A_d is required to be positive, and a conservative uniform prior of $[-4, -2]$ is imposed on α_d based on measurements in the literature (Miville-Deschênes et al. 2016; Planck Collaboration XI 2020).

An example fit to a WISE W3×ACT f150 *TT* spectrum is presented in Figure 4. This region, tile 236, is centered on Galactic longitude $l = 134.^\circ5$ and Galactic latitude $b = -52.^\circ2$ and transitions from being dominated by a Galactic dust spectrum at low-$\ell$to an extragalactic spectrum at high-ℓ. The Galactic component is best fit with $\alpha_d = -2.8 \pm 0.2$, and overall, the parametric model provides an excellent fit to the data ($\chi^2 = 9.6$ for 20 degrees of freedom). Overall, the model provides a good description of the data in all regions. As illustrated in Figure 5, the distribution of χ^2 values across all 107 regions at both f150 and f220 is broadly consistent with expectations, though some outliers have high χ^2 values.

Another visualization of the model fit to all 107 regions is presented in Figure 6, which plots the best-fit Galactic dust amplitude A_d (see Equation (3)) against the measured $\ell = 9000$ bandpower. In high column density regions (large A_d), the high-ℓ spectrum is dominated by Galactic dust emission, and there is a strong linear correlation between $C^{TT}_{\ell=9000}$ and A_d. As A_d decreases to lower column densities, however, $C^{TT}_{\ell=9000}$ asymptotes to a roughly constant value in both f150 and f220. This is the extragalactic signal common to all regions. The sum of the Galactic and extragalactic model components, plotted in black lines assuming $\alpha_d = -3$, provides a good description of the measurements.

Although the model fits are generally good, Figure 5 demonstrates that the distribution of χ^2 values is biased toward higher values than expected. Twelve regions in f150 and nine in f220 have fits with PTE $< 1\%$. We identify two possible explanations for the model failures: (1) Galactic dust *TT* spectra that differ from a pure power law and (2) unmasked compact Galactic sources. Of the 38 (31) regions with PTE $< 10\%$ ($\chi^2 > 25$) in f150 (f220), 18 (14) are regions where departures from the model are mostly at $\ell < 3000$, while the remaining 20 (17) are mostly at $\ell > 3000$.

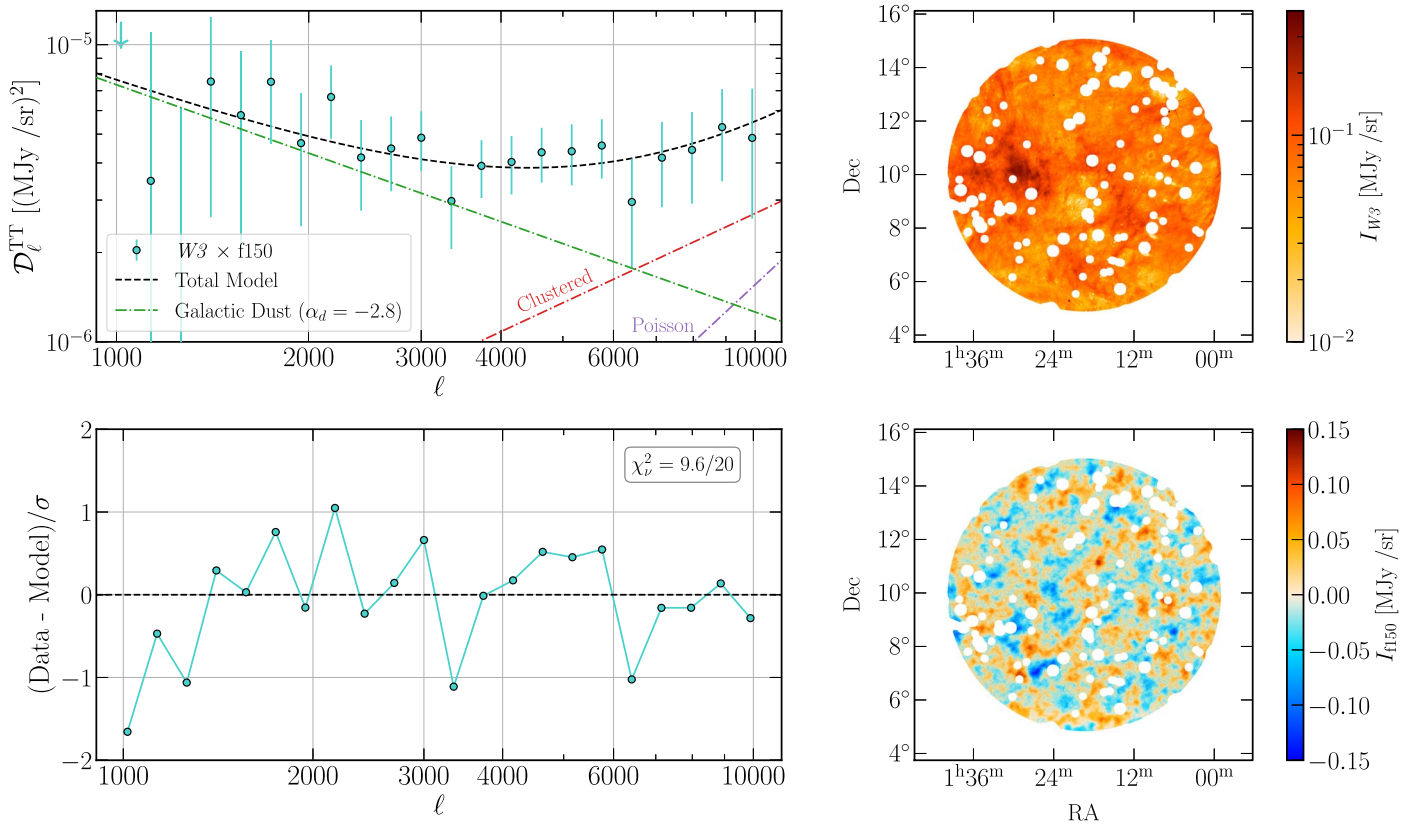

Figure 4. Example model fit of the WISE W3×ACT f150 *TT* spectrum in a moderately high-latitude region ($l = 134.^\circ5$, $b = -52.^\circ2$; Meisner & Finkbeiner 2014; tile 236). The top left panel shows the measured *TT* spectrum (blue circles with error bars) where 2σ upper limits are quoted for bandpowers consistent with zero. Also shown is the total fit model (black) with its region-specific best-fit Galactic dust component (green), along with the global best-fit CIB-C and CIB-P components in red and purple, respectively. The residuals of the fit are presented in the bottom left panel. The top and bottom right panels show the WISE and ACT maps of the region, respectively, including the applied mask. The *TT* spectrum transitions from Galactic emission at low-ℓ to extragalactic emission at high-ℓ and is well fit by the model.

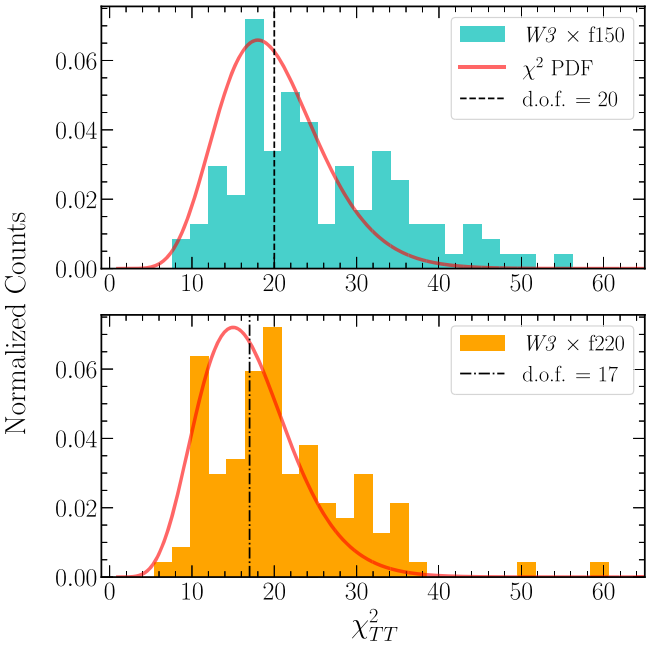

Figure 5. Normalized histograms of χ^2 values for the model fits to all 107 regions at f150 (top) and f220 (bottom). The number of degrees of freedom is indicated with the black dashed line, 20 for f150 and 17 for f220 due to the higher $\ell_{\rm min}$, while the red solid line is the χ^2 PDF for the indicated number of degrees of freedom.

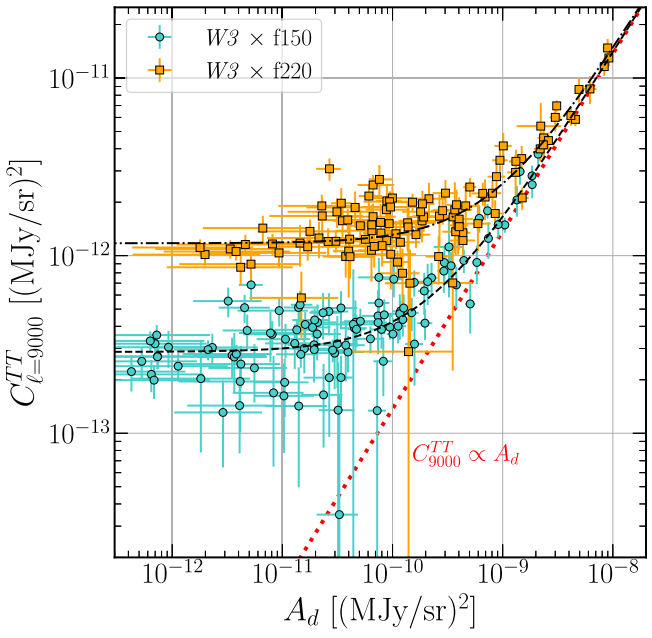

Figure 6. The measured C_ℓ^{TT} at $\ell = 9000$ at f150 (teal circles) and f220 (orange squares) in each of the 107 regions is plotted against the fitted A_d. The red dotted line is $A_d(9000/1000)^{-3}$, corresponding to the Galactic dust term of Equation (3) for $\alpha_d = -3$. The black lines correspond to Equation (3) with $\alpha_d = -3$ and extragalactic parameters at f150 (dashed) and f220 (dashed–dotted) from Table 1. The model provides a good description of the data at both frequencies.

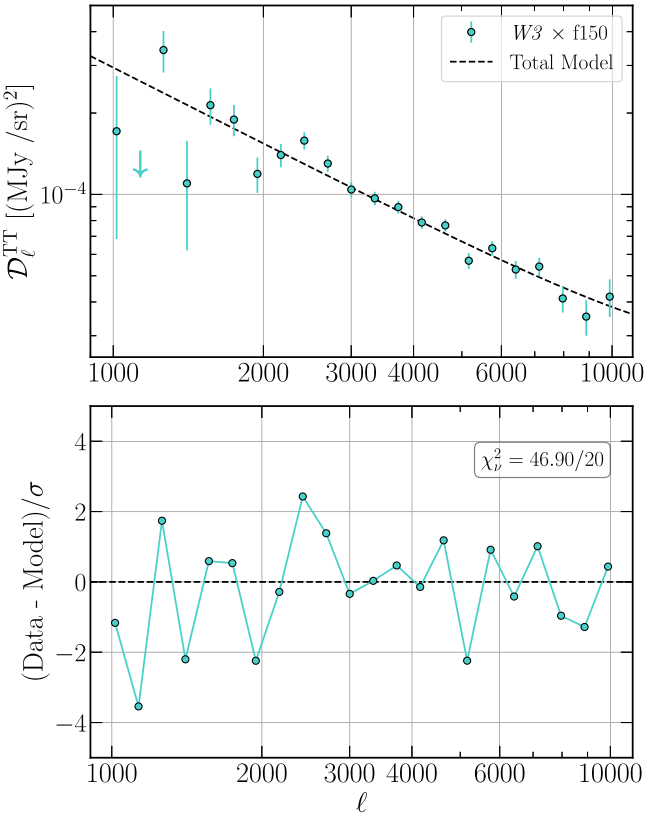

Figure 7. The top panel presents a WISE W3×ACT f150 *TT* spectrum of a region near the Galactic plane ($\ell = 193°$, $b = -15°$) where the model fit (black dashed) is poor (PTE = 0.06%). Down arrows indicate 95% upper limits on bandpowers consistent with zero. The fit residuals are in the bottom panel, demonstrating breakdown of the power-law parameterization at $\ell < 3000$.

We illustrate an example of explanation 1 in Figure 7, which presents the W3×f150 spectrum of a region near the Galactic plane ($b = -15°$). While the $\ell > 3000$ spectrum is well fit by a power law ($\alpha_d = -2.93 \pm 0.04$), there are clear departures at lower multipoles. Indeed, the PTE of the fit is only 0.06%. The relatively high column density of the region permits high signal-to-noise ratio measurements even at $\ell = 10^4$; thus, deviations from our simple parametric model are easier to detect. Further, this region includes a range of dense, complex Galactic structure likely at different distances, so it is not unexpected that the spatial statistics are complicated. Thus, at least in some regions, we appear to be seeing the inability of the model to capture the complexity of the dust emission. We discuss the implications of this further in Section 6.2.

While explanation 1 represents a limitation of the model, explanation 2—the presence of Galactic sources in the maps—is a limitation of the analysis. Sources such as stars, planetary nebulae, and supernova remnants have been identified in ACT maps (Naess et al. 2020), and many of these have counterparts in the WISE maps. While we have used maps that are as cleaned of these objects as possible (see Section 2), residual correlations from objects below our flux cuts could contribute power, particularly at highℓ. Given the robustness of the extragalactic background model fit across a wide range of column densities and Galactic latitudes (see Figure 6), it is unlikely that such sources constitute much of the signal we have identified as extragalactic. However, they could account for regions with high-ℓ power in excess of our model. Higher-fidelity modeling of diffuse dust emission will almost certainly require a dedicated effort to identify and mask Galactic sources at lower flux thresholds than employed here.

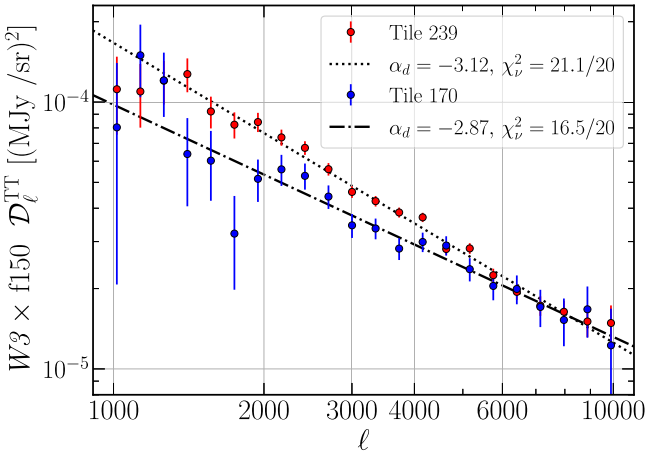

Figure 8. WISE W3×ACT f150 *TT* spectra in two regions (Meisner & Finkbeiner 2014 tiles 170 and 239, located at Galactic latitudes $b = -24.^\circ8$ and $-38.^\circ2$, respectively). The best-fit CIB model has been subtracted from each, and the best-fit Galactic dust models are presented as dashed lines. Notably, the measured power-law index of the Galactic dust *TT* spectrum (α_d) differs between these tiles at $\sim 3\sigma$ significance (-2.87 ± 0.07 vs. -3.12 ± 0.03).

4.3.2. *Variation in Galactic Dust* TT *Spectrum*

We have demonstrated that the model of Equation (3) provides a good description of the *TT* spectrum of most of the 107 regions analyzed here. Although we fit for α_d in each region individually, Figure 6 illustrates that a constant $\alpha_d = -3$ yields a reasonable fit to the data. In this section, we demonstrate that there is true α_d variability in our sample, justifying our choice of fitting α_d as a free parameter and having implications for modeling the dust *TT* spectrum more broadly.

Figure 8 illustrates an example of variation in the slope of the W3×f150 dust *TT* spectrum between two regions. MF14 tiles 170 and 239, both at moderate Galactic latitudes ($b = -24.^\circ8$ and $-38.^\circ2$, respectively), have comparable *TT* power at $\ell \gtrsim 6000$. However, at lower multipoles, they diverge. The best-fit α_d values for the two regions are -3.12 ± 0.03 and -2.87 ± 0.07, respectively. The W3×f220 *TT* spectra of these two regions are best fit by α_d values of -3.13 ± 0.04 and -2.86 ± 0.08, respectively.

The distribution of the best-fit α_d values is presented in Figure 9, which shows the best-fit α_d in f150 against the best-fit value at f220 for 29 regions with $A_d/\sigma(A_d) > 5$ at both frequencies. The best-fit values for α_d range from -3.4 to -2.7. In these 29 regions, we find a median $\alpha_d = -2.95$ and -2.96 at f150 and f220, respectively, while the α_d values at the two frequencies are correlated at a level of Pearson $r = 0.5$. To assess the statistical significance of region-to-region variation in α_d, we consider two models: (1) α_d is constant over all regions and is estimated as the inverse variance weighted mean of the 58 α_d values in the 29 regions at the two frequencies, and (2) α_d differs from region to region and is estimated in each region as the weighted mean of the two α_d fits at f150 and f220. Model 1 has $\chi^2 = 151$ for 57 degrees of freedom, while model 2 has $\chi^2 = 37$ for 29 degrees of freedom. The likelihood ratio test assuming the α_d posteriors are Gaussian yields a 7σ preference for the model with region-to-region α_d variations.

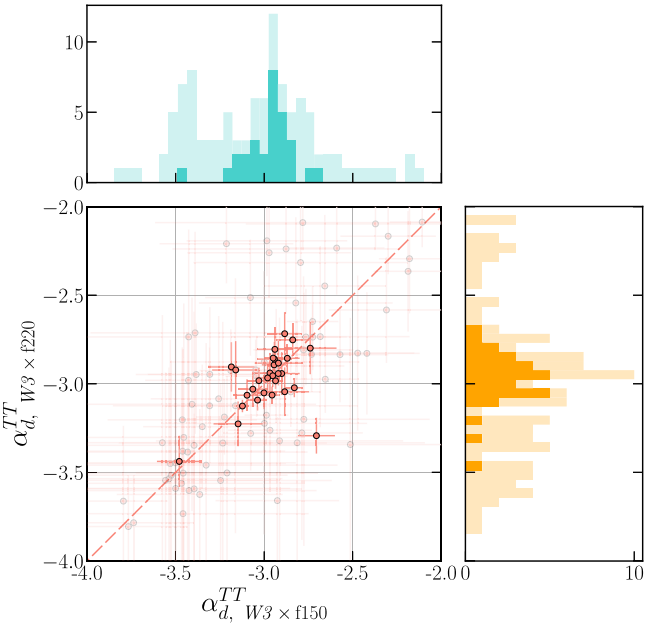

Figure 9. The α_d^{TT} slopes and uncertainties estimated from WISE W3×ACT [150, 220] GHz. Regions with >5σ detections of Galactic dust A_d^{TT} in both frequencies are opaque. The dashed line shows the one-to-one line. Histograms show the distribution of α_d for the two frequencies, where >5σ measurements of A_d^{TT} are opaque. The dust spectral indices are correlated between f220 and f150.

The model with constant α_d has a PTE of 2×10^{-10}, corresponding to exclusion at 6σ significance.

The correlation of the fitted α_d values between f150 and f220 is consistent with true astrophysical variations in the value of α_d. However, some of the variation could be driven by a fitting degeneracy between the amplitudes of the Galactic component and the extragalactic signal. We find that α_d is negatively correlated with column density, i.e., with shallower slopes at low column densities. This behavior is as predicted by a fitting degeneracy but is not inconsistent with astrophysical variation. The 5σ cut employed above mitigates the effect of this fitting degeneracy on our analysis of α_d variations. If these are indeed physical variations, they could be confirmed with other tracers.

5. Polarization Analysis

In this section, we analyze the cross-power spectra between the W3 total intensity map and millimeter polarization maps at 150, 220, and 353 GHz, focusing on the *TE* spectra. Unlike the *TT* analysis in Section 4, for the *TE* analysis, we employ ACT maps that have been coadded with Planck data (Naess et al. 2020) to enhance the signal-to-noise ratio at $\ell\lesssim2000$ (see Section 2.1 for details).

We present a sample of nine of the highest signal-to-noise ratio W3×f150 *TE* spectra in Figure 10. In all nine regions, $\mathcal{D}_\ell^{TE}>0$ over most or all of the ℓ range considered ($10^3<\ell<10^4$).

We first check if systematic temperature-to-polarization leakage in the ACT maps could bias our measurement of *TE*. Following Lungu et al. (2022), the expected $T\rightarrow E$ leakage is modeled as a leakage beam $B_\ell^{T\rightarrow E}$ that is determined from ACT *Q* and *U* maps of Uranus. To first order, the expected bias to the *TE* spectrum is given by $C_\ell^{TT}B_\ell^{T\rightarrow E}/B_\ell$, where C_ℓ^{TT} is the measured WISE×ACT cross-spectrum, and B_ℓ is the instrumental beam. The leakage signal is found to be largest in f220 and peaks at the highest multipoles included our analysis ($\ell\sim4000$), but it is still $\lesssim$1% of the measured *TE* signal. We therefore ignore the systematic $T\rightarrow E$ leakage in the analysis.

We next apply the data model in Equation (5) to characterize the spectra of all 107 regions. In our fiducial analysis, we use a uniform prior on A_d and fix $\alpha_d^{TE}=-2.5$, representative of measurements over large sky areas at $40<\ell<600$ (Planck Collaboration XI 2020). We fit over the range $10^3<\ell<10^4$ for both f150 and f220. We repeat the analysis with Planck 353 GHz data but restrict the fits to $1000<\ell<2000$ given the lack of constraining power of the Planck polarization data at higher multipoles.

The fits to the W3×f150 *TE* spectra of the nine selected regions presented in Figure 10 demonstrate broad but imperfect agreement with a power-law model. In all cases, $A_d^{TE}>0$ with $A_d^{TE}/\sigma(A_d^{TE})>3$, indicating robust detections of a positive *TE* signal in all nine regions. Figure 11 shows the $A_d^{TE}/\sigma(A_d^{TE})$ values of all regions as a function of Galactic latitude. In total, there are 26 regions with $A_d^{TE}/\sigma(A_d^{TE})>3$ for f150, 17 regions for f220, and 13 regions with $A_d^{TE}/\sigma(A_d^{TE})>3$ in both f150 and f220. Most significant detections of nonzero *TE* signal are in regions at $|b|<40°$, where the dust emission is brightest. There are no regions in which $A_d^{TE}<0$ at 3σ significance at either frequency. The distribution of fitted A_d^{TE} values is clearly biased toward $A_d^{TE}>0$.

In detail, however, the *TE* spectra are not all well described by a power law in ℓ. The χ^2 distributions of the ensemble of f150 and f220 fits are presented in Figure 12. Agreement with the expected χ^2 probability density function (PDF) is generally good, but there are more regions with large χ^2 values than expected from chance. Allowing α_d^{TE} to vary yields only marginal improvements in most regions, suggesting that the data have little constraining power on the *TE* spectral index.

The shape of the *TE* power spectrum may vary because of the structure of the diffuse dust emission itself, which is not necessarily well described by a power law in ℓ. On the other hand, the measured *TE* power spectrum may be affected by any compact sources in the map that were not identified by the MF14 flags. Further, the WISE data still contain a number of unmitigated data artifacts that could also affect the spectra, particularly at high ℓ. Given the limitations imposed by these potential systematics and the lack of evidence for variability in α_d^{TE}, we do not draw strong conclusions on the shape of the *TE* spectra.

Applying our fitting framework to the Planck 353 GHz data yields 19 regions with $A_d^{TE}>0$ at 3σ confidence. Five of these nonzero *TE* detections are unique to the 353 GHz analysis, while the remaining regions were identified with f150 (11), f220 (11), or both (8). To assess the impact of the Planck data in the ACT+Planck coadds, we repeat the f150 and f220 fits over the multipole range $2000<\ell<10^4$, where the Planck data have little constraining power. We find that the number of 3σ positive *TE* detections falls from 26 to 17 for f150 and from 17 to 5 for f220.

As further illustration of the relative constraining power of the three frequencies on the *TE* spectrum, Figure 13 presents the f150, f220, and Planck 353 GHz *TE* spectra of tile 239, centered on $(l,\ b)=(172.^\circ2,\ -38.^\circ2)$. To facilitate direct comparison, we scale the f220 and 353 GHz spectra to 150 GHz assuming a modified blackbody emission law with $\beta=1.5$ and $T_d=20$ K. The Planck 353 GHz spectrum is truncated at $\ell=2000$ due to a lack of sensitivity at higher multipoles. There is broad agreement in the amplitude (after

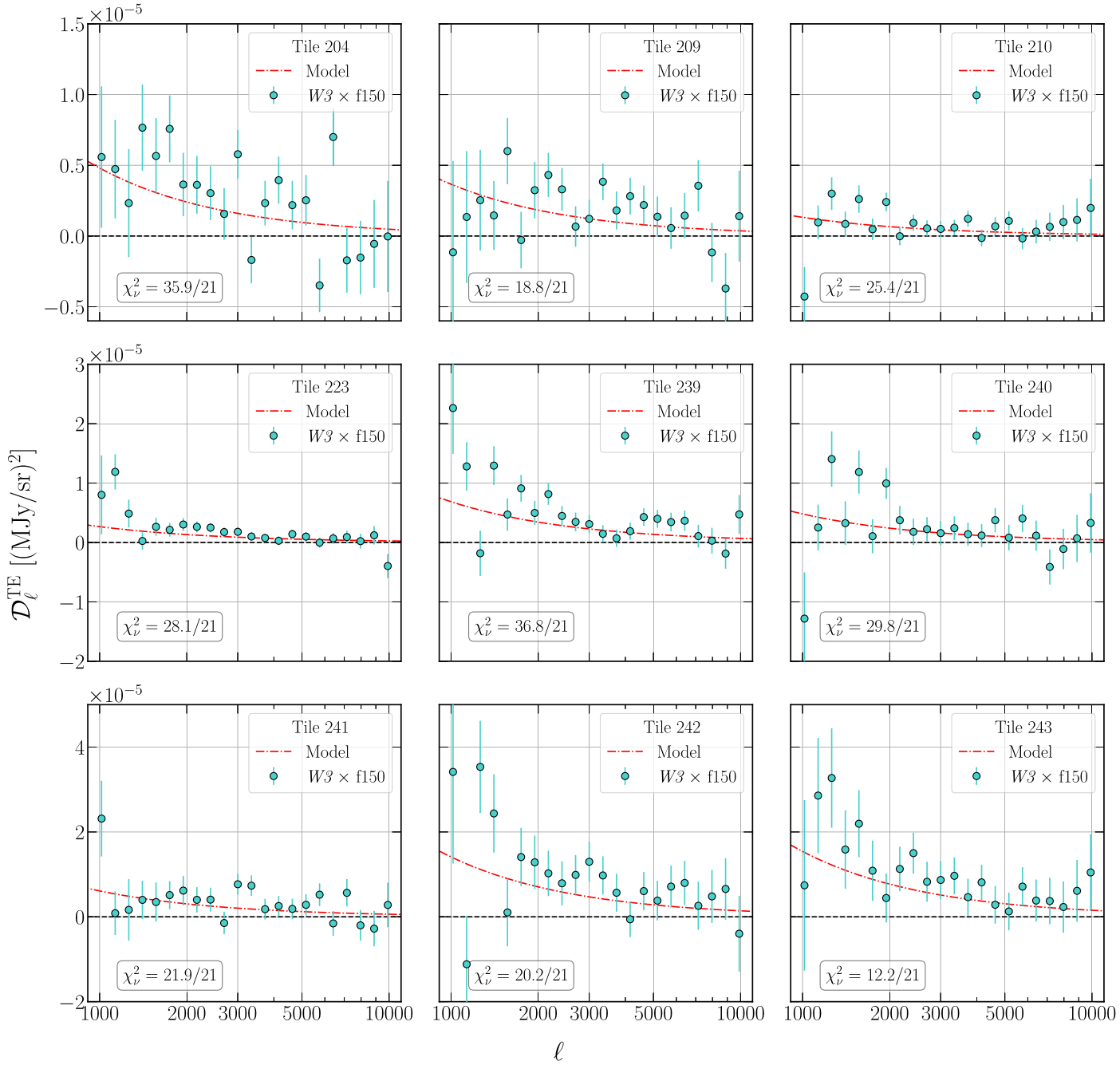

Figure 10. A selection of the highest signal-to-noise ratio W3×f150 *TE* spectra. The best-fit power law $C_\ell^{TE} \propto \ell^{-2.5}$ is shown (red dashed) along with its associated χ^2 value.

scaling) and shape of the *TE* spectrum across the three frequencies. The ACT data are consistent with positive C_ℓ^{TE} out to scales $\ell \simeq 6000$. To our knowledge, these are the smallest-scale measurements of a Galactic dust *TE* spectrum to date. Using the Capitanio et al. (2017) 3D reddening map, we estimate that the dust emission toward the center coordinates of tile 239 primarily originates from a distance of about 150 pc from the Sun. At 150 pc, our measurements constrain the dust *TE* down to physical scales of ∼0.05 pc.

The fitted A_d^{TE} values are highly correlated with the fitted A_d^{TT} values, as expected. However, we find that the relation between these quantities is sublinear; A_d^{TE} scales roughly as $(A_d^{TT})^{0.8}$. Two physical effects may contribute to this relation. First, as the dust column density increases, so too does the number of distinct structures that may be superimposed along the line of sight. While the *TT* correlation is unaffected by such superposition, the *TE* correlation may be weakened by depolarization and by loss of apparent filamentarity in the integrated map. Second, at higher column densities, a loss of alignment between the local magnetic field and dust filaments is observed (Planck Collaboration Int. XXXII 2016). This should weaken the *TE* correlation, which is positive in diffuse regions due to a preferred alignment between dust structures and the magnetic field (Planck Collaboration Int. XXXVIII 2016; Clark et al. 2021).

We repeat this analysis on the *TB* spectra, finding no 3σ detections of nonzero *TB* in any region. The fitted A^{TB}

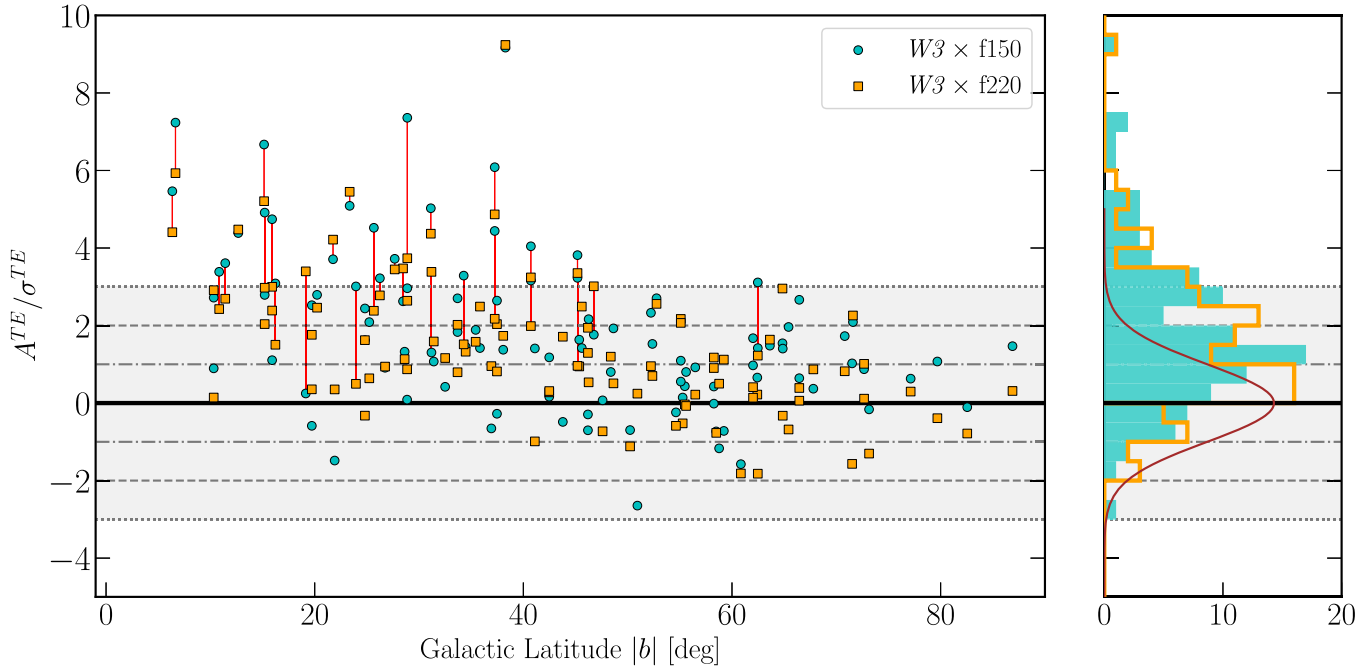

Figure 11. Left: the best-fit A_d^{TE} (see Equation (5)) in each of the 107 regions for each of f150 and f220 shown as a function of Galactic latitude. The A_d^{TE} have been normalized by the uncertainty of the fit. Vertical red lines connect selected pairs of f150 and f220 values for the same region. Right: histogram of A_d^{TE}/σ^{TE} with a unit Gaussian overlaid in dark brown, illustrating bias toward positive *TE*.

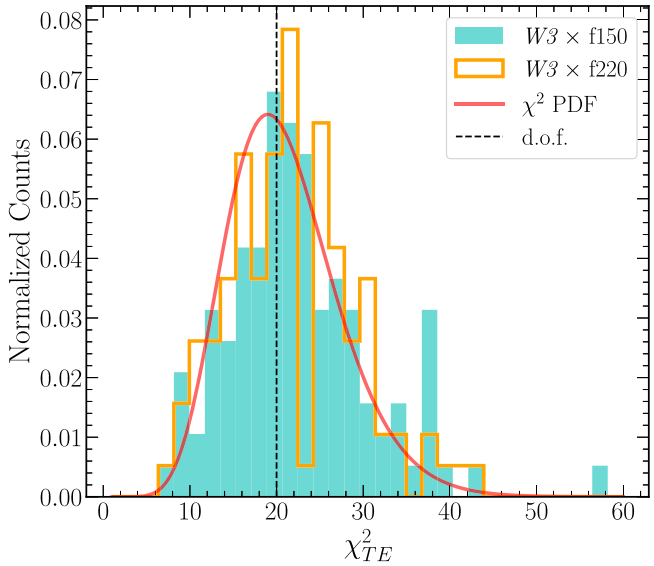

Figure 12. Distribution of χ^2 values across all regions for the fits employing Equation (5). While a simple power-law model $C_\ell^{TE} \propto \ell^{-2.5}$ is broadly consistent with the data, there is evidence for departures.

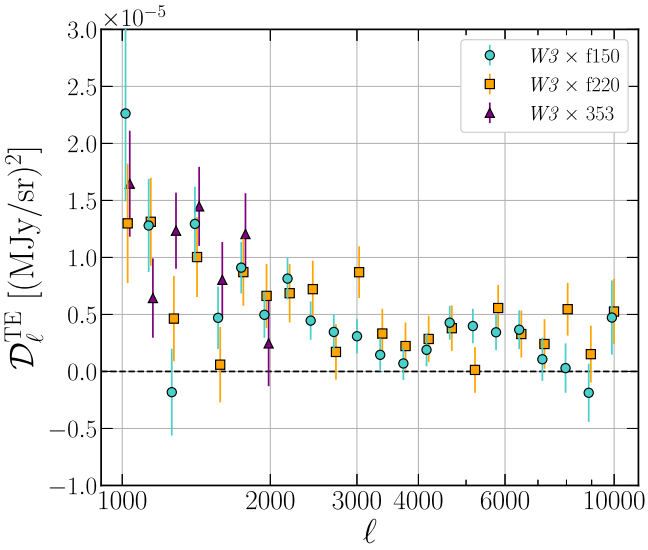

Figure 13. A comparison of the W3×f150, f220, and Planck 353 GHz *TE* spectra of tile 239 ($(l, b) = (172.^\circ2, -38.^\circ2)$). The f220 and 353 GHz spectra have been scaled to 150 GHz assuming a modified blackbody spectral energy distribution with $\beta = 1.5$ and $T_d = 20$ K, corresponding to multiplicative factors of 0.286 and 0.065, respectively. The Planck 353 GHz spectrum is truncated at $\ell = 2000$ due to the lack of Planck sensitivity at higher multipoles. The three spectra are broadly consistent in amplitude (after scaling) and shape over the full ℓ range shown.

amplitudes at both f150 and f220 are compared to the A^{TE} amplitudes in Figure 14. Unlike the fitted A^{TE}, the ensemble of A^{TB} amplitudes show no bias toward positive or negative values at either frequency.

6. Discussion

6.1. MIR PAH Emission as a Spatial Template for Microwave Dust Emission

Measurements of the CMB at small (∼arcminute) angular scales is a principal focus of current and upcoming ground-based experiments. Measurements of lensing of the CMB constrain the growth of structure in the Universe and the neutrino masses, while removal of the *B*-mode signature generated by lensing will be required for constraints on primordial *B*-mode signatures at the levels pursued by next-generation experiments. Critical to all of these analyses is robustness to Galactic emission at small angular scales. As the combination of sensitivity and angular resolution does not yet exist to characterize millimeter-wavelength dust emission at

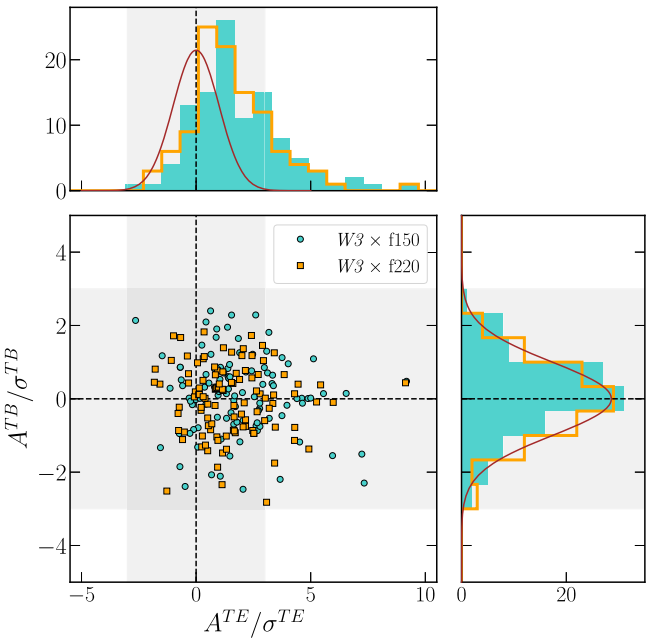

Figure 14. Best-fit A_d values (see Equation (5)) for *TE* (*x*-axis) and *TB* (*y*-axis) in each of the 107 regions at both f150 and f220. Both quantities have been normalized by the 1σ uncertainty of the fit, with the shaded regions corresponding to $\pm 3\sigma$. Also shown are the corresponding histograms with a unit Gaussian overlaid in dark brown. The distribution of A^{TE} (top) is biased positive (as seen in Figure 11), but the distribution of A^{TB} (right) shows no significant trend.

these scales directly, indirect probes of these dust properties are needed.

We have demonstrated that the WISE W3 measurements of Galactic dust emission correlate with both total and polarized intensity millimeter-wave observations at scales $10^3 < \ell < 10^4$. Further, the slope of the measured *TT* spectrum is compatible with *TT* spectra measured from millimeter data only at lower multipoles. The WISE data therefore offer a means of characterizing the spatial structure of Galactic dust emission, including non-Gaussianity, that will be informative for millimeter-wavelength analyses.

While this is a promising direction for future analysis, we highlight a few caveats. W3 primarily traces emission from PAHs, which are known to differ in both emission physics and spatial distribution from the submicron grains responsible for the bulk of the millimeter emission. The fraction of the dust mass in PAHs is variable throughout the Galaxy, with fewer PAHs per unit dust mass found in very dense regions, H II regions, and the warm neutral medium (WNM). Because PAHs undergo single-photon heating, their emission scales with the first power of the energy density of the interstellar radiation field U. In contrast, millimeter-wavelength emission from submicron grains scales as $U^{1/4+\beta} \simeq U^{1/5.5}$. Thus, to the extent that the radiation field heating the dust varies across the sky, the ratio of PAH emission to millimeter dust emission likewise varies. On the other hand, the availability of two independent probes of U could help constrain spatial variations in the dust temperature and thus frequency decorrelation, a key concern for *B*-mode analyses.

6.2. Variability of the Dust Power Spectrum

Simulated maps of Galactic emission used in CMB analyses frequently assume that the Galactic dust *B*-mode spectrum is a power law in ℓ (e.g., Hervías-Caimapo et al. 2016; Thorne et al. 2017). Measurements with the Planck satellite demonstrate this to be a good approximation over large sky areas for $40 < \ell < 600$, with $C_\ell^{BB} \propto \ell^{-2.5}$ (Planck Collaboration XI 2020). In detail, however, the dust power spectrum is expected to vary in slope across the sky. For instance, Marchal & Miville-Deschênes (2021) found that the steepness of the dust *TT* spectrum is influenced by the filling factor of the WNM on the line of sight.

We have shown evidence of spatial variability in the steepness of the dust *TT* spectrum at arcminute scales. Further, we find that some of the *TT* spectra are not well described by power laws at all. The spatial distribution of Galactic dust is complex, and it is unsurprising that a power law in ℓ is an inadequate description of the power spectrum. If this variability indeed arises from the spatial inhomogeneity of interstellar density structures and the magnetohydrodynamic turbulence that shapes them, then a corresponding variability is expected in polarization, including the dust *TE* and *BB* spectra. Detailed constraints on the shape of the dust *TE* spectrum and its variations within the Galaxy will be possible with more sensitive polarization data.

The observed spatial variations in the dust power spectrum underscore the need for scrutiny of simple power-law models for the scale dependence of Galactic dust emission. Moment-based methods (Chluba et al. 2017; Vacher et al. 2023) can account for deviations from power-law behavior in ℓ (e.g., Azzoni et al. 2021) and could be tested on the regions identified here.

A challenge for both the analysis presented in this work and for dust modeling in a CMB foregrounds context is the presence of compact sources. In addition to extragalactic sources, we have identified a number of Galactic sources, such as planetary nebulae, having strong emission at both MIR and millimeter wavelengths. If left unmasked, these sources can strongly affect the measured power spectra at high ℓ. While we have employed aggressive masking (as described in Section 3.2), sources below the ACT flux density cut may still contribute nonnegligible power. Dedicated identification and characterization of such sources will be the topic of future work.

6.3. *Dust* TE *and* TB *Correlations at Arcminute Scales*

Over large regions of sky and on large angular scales, the dust total intensity is positively correlated with the dust *E*-mode polarization (Planck Collaboration Int. XXX 2016; Planck Collaboration XI 2020). This positive *TE* correlation is consistent with a preferential alignment between elongated dust intensity structures and the plane-of-sky projected magnetic field orientation traced by polarized dust emission (Planck Collaboration Int. XXXVIII 2016). This magnetically aligned density anisotropy is also seen in H I and additionally provides a natural explanation for the observation that the dust polarization $EE/BB > 1$ (Clark et al. 2015). Filament-based models of Galactic dust polarization that invoke this alignment also show $TE > 0$ (Clark & Hensley 2019; Hervías-Caimapo & Huffenberger 2022).

If magnetically aligned ISM filaments source the observed positive *TE* correlation, this raises several observationally measurable questions, in particular, whether and how *TE* correlation changes as a function of scale and/or Galactic environment. There could be an environmental *TE* dependence

set by the relative orientation of filaments and magnetic fields in regions dominated by different physics. Filamentary structures are strongly aligned with the magnetic field orientation throughout the diffuse ISM (Clark et al. 2014), but higher-density filaments are closer to being orthogonal to the projected magnetic field orientation (Planck Collaboration Int. XXXII 2016; Planck Collaboration Int. XXXV 2016; Fissel et al. 2019b). This empirical result may be related to the mass-to-flux ratio of molecular cloud filaments (e.g., Seifried et al. 2020).

A dust filament with a polarization structure that corresponds to a perpendicular plane-of-sky magnetic field orientation would produce a negative *TE* correlation (Zaldarriaga 2001; Huffenberger et al. 2020). The diffuse outskirts of molecular clouds, bright in PAH emission, often have magnetic field orientations that are orthogonal to the main molecular filament (e.g., Chapman et al. 2011; Malinen et al. 2016), so we might expect negative TE correlations toward higher column density regions. We find that the measured *TE* correlation is generally stronger at higher column densities and lower Galactic latitudes, where the dust is brighter and measured with a higher signal-to-noise ratio, but even at low Galactic latitudes, we find no robust detections of negative *TE* spectra (Figure 11). The data are thus consistent with a general alignment between the ACT-measured magnetic field and the density structures seen in PAH emission. The scale dependence of the *TE* correlation is plausibly related to the physics that couples the dust density structure to the magnetic field on a particular scale. This work measures dust *TE* that is generally biased toward positive values down to subparsec scales.

Planck data also exhibit a nonzero *TB* correlation over large sky areas and large angular scales (Planck Collaboration Int. XXX 2016; Planck Collaboration XI 2020). In the filament-based model, nonzero *TB* is caused by imperfect alignment between the long axis of a dust filament and the magnetic field, such that nonzero *TB* over large sky regions implies that this misalignment has a preferred handedness (Huffenberger et al. 2020; Clark et al. 2021; Cukierman et al. 2023). In cross-correlation with the WISE data, we find no regions with robustly nonzero *TB* and no preference for one sign of *TB* over the distribution of sky regions considered.

6.4. The Cosmic PAH Background

We have detected at 30σ significance a high-ℓ correlation between the W3 map at 12 μm and the f150 and f220 ACT maps inconsistent with extrapolation of the Galactic dust power spectrum. The correlation appears spatially isotropic and well described as a power law $C_\ell \propto \ell^{-1}$. We conclude that this signal is extragalactic in origin and most likely to arise from the correlation between PAH emission in dusty, star-forming galaxies as seen by WISE and the CIB as seen by ACT.

The rest-frame MIR emission of a dusty star-forming galaxy is dominated by PAH features that can account for up to ~20% of its total infrared emission (Smith et al. 2007). The strongest of these is the 7.7 μm feature (Tielens 2008). Even at $z = 0$, this feature makes a nonnegligible contribution to the W3 band, and it remains within the W3 band up to $z \simeq 1$. Using large optical galaxy catalogs, Chiang & Ménard (2019) demonstrated that the MF14 map is correlated with galaxies in redshift bins up to $z \sim 2$, consistent with redshifted PAH emission. Detailed modeling of the extragalactic background light suggests that the 12 μm extragalactic sky is dominated by PAH emission from star-forming galaxies rather than by emission associated with AGN (e.g., Andrews et al. 2018). Likewise, in recent multiwavelength fits to galaxies detected by ACT, Kilerci et al. (2023) found that even galaxies dominated by AGN emission at ACT frequencies could be dominated by PAH emission at 12 μm. Thus, the "cosmic PAH background" appears to be the most natural explanation for the observed correlation, though we cannot rule out significant contributions from a 12 μm "cosmic AGN background" on the basis of these data alone.

The cross-power spectrum encodes the relationship between the galaxies producing the MIR and millimeter-wavelength emission. We find that the correlation is inconsistent with a pure Poisson spectrum, but, as illustrated in Figure 3, the relative contributions of a clustered versus Poisson component are not well constrained. Previous measurements of the CIB at submillimeter wavelengths have found that the Poisson component dominates the signal at $\ell \gtrsim 2000$ (Dunkley et al. 2013; Viero et al. 2013; Béthermin et al. 2017). It is plausible that the MIR emission in W3 traces a galaxy population that is distinct from but spatially clustered with the galaxy population observed in the submillimeter, leading to a subdominant Poisson component in the W3×f150 and W3×f220 cross-spectra. Interpretation of the shape of the power spectrum would benefit from forward models of the cosmic PAH background based on galaxy simulations.

The frequency spectrum of the emission, both in the MIR and at millimeter wavelengths, is a window into galaxy properties. Similarly, quantification of the level of correlation of maps of diffuse extragalactic emission at two frequencies constrains the diversity of emission spectra and their variability with galaxy properties and cosmic time. For instance, with a greater number of MIR bands, it will be possible to assess whether different PAH features preferentially arise from galaxies with different properties. Likewise, the level of correlation between MIR and millimeter-wavelength maps constrains the extent to which it is the same population of galaxies responsible for the observed emission in both frequency ranges. Ultimately, the implementation of PAH emission spectra in tools such as SIDES (Béthermin et al. 2017) and Websky (Stein et al. 2020) could allow these data to place constraints on the relationship between PAH-bright galaxies and those responsible for the CIB, including how the PAH luminosity function evolves with cosmic time.

In addition to extragalactic emission, the observed high-ℓ correlation could also include a contribution from Galactic point sources. Large numbers of dusty, compact Galactic point sources have been identified in Planck data (Planck Collaboration XXVIII 2016), and ACT has observed objects such as planetary nebulae that are also bright in the W3 band (Naess et al. 2020). While we see no evident correlation between the high-ℓcomponent we model as extragalactic emission and Galactic latitude or dust column density, careful treatment of Galactic contamination will be required to make quantitative comparisons between the signal observed here and models of extragalactic emission.

7. Conclusions

We have presented a correlation analysis between 12 μm emission observed by WISE and both 150 and 220 GHz emission observed by ACT at multipoles $10^3 < \ell < 10^4$. Our principal conclusions are as follows.

1. We report a 30σ detection of a spatially isotropic, high-ℓ *TT* signal that we interpret as a correlation between the CIB at ACT frequencies and the cosmic PAH background seen by WISE. The spectrum is well fit by a power law $C_\ell \propto \ell^{-1}$, consistent with a clustered component. The fits do not require, but also do not exclude, the presence of a Poisson component.
2. The *TT* spectrum of Galactic dust at $10^3 < \ell < 10^4$ is generally well fit by a power law in ℓ with $C_\ell^{TT} \propto \ell^{-2.9}$, consistent with Galactic dust *TT* spectra that have been measured at lower multipoles (e.g., Gautier et al. 1992; Bracco et al. 2011; Hajian et al. 2012; Planck Collaboration XXX 2014). However, we find evidence for spatial variability in the power-law index and identify several regions where a power law is an inadequate description of the *TT* spectrum at the sensitivity of the measurements. The strength of the observed correlation suggests that WISE maps of dust emission can be used to understand the spatial statistics of millimeter-wavelength dust emission at small angular scales.
3. We identify 35 regions with $>3\sigma$ detections of positive *TE* correlation and none with $>3\sigma$ detections of negative *TE* correlation. We further find that the distribution of all fit *TE* amplitudes is biased positive. To our knowledge, these are the highest-ℓ measurements of the dust *TE* correlation to date.

This work showcases the power of high angular resolution observations of dust emission at MIR wavelengths to understand the astrophysics of dust emission at millimeter wavelengths. The small-scale dust morphology in the WISE maps may be representative of what will be observed by next-generation millimeter experiments, so characterization of its non-Gaussianity and other properties is a promising direction for future work.

The cosmic PAH background provides another window into the evolution of galaxies with cosmic time, especially the buildup of PAHs. Implementation of PAH spectra into existing tools to model the CIB and cross-correlating the cosmic PAH background with other tracers of galaxy properties (e.g., H I emission) will be important for understanding the properties of the galaxies giving rise to this emission. Given the recent JWST detection of the 2175 Å feature associated with PAHs in a $z = 6.71$ galaxy (Witstok et al. 2023), understanding how the Universe becomes enriched with PAHs is all the more pressing.

The data underlying the analyses in this work are set to improve dramatically in the near future. The Simons Observatory will soon begin operations in Chile and will provide maps of millimeter dust emission and polarization with greater sensitivity and over a wider frequency range than ACT (Ade et al. 2019; Hensley et al. 2022). The SPHEREx satellite will soon measure the full sky at $\sim 6''$ angular resolution in 102 channels spanning 0.75–5 μm, each with comparable sensitivity to WISE (Crill et al. 2020). From the cosmic PAH background to the morphology of dust throughout the Milky Way, these new data sets can be used to extend the investigations presented here.

Acknowledgments

We thank B. Draine, D. Finkbeiner, J. Greene, A. Goulding, A. Meisner, M. A. Miville-Deschênes, and D. Spergel for helpful conversations and guidance throughout the course of this work. Support for ACT was through the U.S. National Science Foundation through awards AST-0408698, AST-0965625, and AST-1440226 for the ACT project, as well as awards PHY-0355328, PHY-0855887, and PHY-1214379. Funding was also provided by Princeton University, the University of Pennsylvania, and a Canada Foundation for Innovation (CFI) award to UBC. ACT operated in the Parque Astronómico Atacama in northern Chile under the auspices of the Agencia Nacional de Investigacion y Desarrollo (ANID). The development of multichroic detectors and lenses was supported by NASA grants NNX13AE56G and NNX14 AB58G. Detector research at NIST was supported by the NIST Innovations in Measurement Science program.

We thank the Republic of Chile for hosting ACT in the northern Atacama and the local indigenous Licanantay communities whom we follow in observing and learning from the night sky.

Computing was performed using the Princeton Research Computing resources at Princeton University. R.C.R. acknowledges support from the Ford Foundation Predoctoral Fellowship from the National Academy of Sciences, Engineering, and Medicine. B.S.H. acknowledges support from NSF grant AST-1908123. S.E.C. acknowledges support from National Science Foundation grant No. AST-2106607. S.K.C. acknowledges support from NSF award AST-2001866. C.S. acknowledges support from the Agencia Nacional de Investigación y Desarrollo (ANID) through FONDECYT grant No. 11191125 and BASAL project FB210003.

Facilities: Planck, WISE.

Software: Astropy (Astropy Collaboration et al. 2013, 2018, 2022), `emcee` (Foreman-Mackey et al. 2013, 2019), Matplotlib (Hunter 2007), `NaMaster` (Alonso et al. 2019), NumPy (van der Walt et al. 2011; Harris et al. 2020), `pixell` (Naess et al. 2021), SciPy (Virtanen et al. 2020).

ORCID iDs

Rodrigo Córdova Rosado https://orcid.org/0000-0002-7967-7676
Brandon S. Hensley https://orcid.org/0000-0001-7449-4638
Susan E. Clark https://orcid.org/0000-0002-7633-3376
Adriaan J. Duivenvoorden https://orcid.org/0000-0003-2856-2382
Zachary Atkins https://orcid.org/0000-0002-2287-1603
Elia Stefano Battistelli https://orcid.org/0000-0001-5210-7625
Steve K. Choi https://orcid.org/0000-0002-9113-7058
Jo Dunkley https://orcid.org/0000-0002-7450-2586
Carlos Hervías-Caimapo https://orcid.org/0000-0002-4765-3426
Zack Li https://orcid.org/0000-0002-0309-9750
Thibaut Louis https://orcid.org/0000-0002-6849-4217
Sigurd Naess https://orcid.org/0000-0002-4478-7111
Lyman A. Page https://orcid.org/0000-0002-9828-3525
Bruce Partridge https://orcid.org/0000-0001-6541-9265
Cristóbal Sifón https://orcid.org/0000-0002-8149-1352
Suzanne T. Staggs https://orcid.org/0000-0002-7020-7301
Cristian Vargas https://orcid.org/0000-0001-5327-1400
Edward J. Wollack https://orcid.org/0000-0002-7567-4451

References

Addison, G. E., Dunkley, J., Hajian, A., et al. 2012, ApJ, 752, 120
Ade, P., Aguirre, J., Ahmed, Z., et al. 2019, JCAP, 2019, 056

Alonso, D., Sanchez, J. & LSST Dark Energy Science Collaboration 2019, MNRAS, 484, 4127
Andrews, S. K., Driver, S. P., Davies, L. J. M., Lagos, C. d. P., & Robotham, A. S. G. 2018, MNRAS, 474, 898
Astropy Collaboration, Price-Whelan, A. M., Lim, P. L, et al. 2022, ApJ, 935, 167
Astropy Collaboration, Price-Whelan, A. M., Sipőcz, B. M., et al. 2018, AJ, 156, 123
Astropy Collaboration, Robitaille, T. P., Tollerud, E. J., et al. 2013, A&A, 558, A33
Azzoni, S., Abitbol, M. H., Alonso, D., et al. 2021, JCAP, 2021, 047
BICEP/Keck Collaboration, Ade, P. A. R., Ahmed, Z., et al. 2023, ApJ, 945, 72
Béthermin, M., Wu, H. Y., Lagache, G., et al. 2017, A&A, 607, A89
Blagrave, K., Martin, P. G., Joncas, G., et al. 2017, ApJ, 834, 126
Bracco, A., Cooray, A., Veneziani, M., et al. 2011, MNRAS, 412, 1151
Bracco, A., Ghosh, T., Boulanger, F., & Aumont, J. 2019, A&A, 632, A17
Capitanio, L., Lallement, R., Vergely, J. L., Elyajouri, M., & Monreal-Ibero, A. 2017, A&A, 606, A65
Chapman, N. L., Goldsmith, P. F., Pineda, J. L., et al. 2011, ApJ, 741, 21
Chiang, Y. K., & Ménard, B. 2019, ApJ, 870, 120
Chluba, J., Hill, J. C., & Abitbol, M. H. 2017, MNRAS, 472, 1195
Clark, S. E., & Hensley, B. S. 2019, ApJ, 887, 136
Clark, S. E., Hill, J. C., Peek, J. E. G., Putman, M. E., & Babler, B. L. 2015, PhRvL, 115, 241302
Clark, S. E., Kim, C. G., Hill, J. C., & Hensley, B. S. 2021, ApJ, 919, 53
Clark, S. E., Peek, J. E. G., & Miville-Deschênes, M. A. 2019, ApJ, 874, 171
Clark, S. E., Peek, J. E. G., & Putman, M. E. 2014, ApJ, 789, 82
Crill, B. P., Werner, M., Akeson, R., et al. 2020, Proc. SPIE, 11443, 114430I
Crovisier, J., & Dickey, J. M. 1983, A&A, 122, 282
Cukierman, A. J., Clark, S. E., & Halal, G. 2023, ApJ, 946, 106
Cutri, R. M., Wright, E. L., Conrow, T., et al. 2012, VizieR Online Data Catalog: WISE All-Sky Data Release (Cutri+ 2012), II/311
Draine, B. T., & Li, A. 2007, ApJ, 657, 810
Draine, B. T., Li, A., Hensley, B. S., et al. 2021, ApJ, 917, 3
Dunkley, J., Calabrese, E., Sievers, J., et al. 2013, JCAP, 2013, 025
Elmegreen, B. G., & Scalo, J. 2004, ARA&A, 42, 211
Ferrière, K. M. 2001, RvMP, 73, 1031
Fissel, L., Hull, C. L. H., Clark, S. E., et al. 2019a, Astro2020: Decadal Survey on Astronomy and Astrophysics, 193
Fissel, L. M., Ade, P. A. R., Angilè, F. E., et al. 2019b, ApJ, 878, 110
Foreman-Mackey, D., Farr, W., Sinha, M., et al. 2019, JOSS, 4, 1864
Foreman-Mackey, D., Hogg, D. W., Lang, D., & Goodman, J. 2013, PASP, 125, 306
García-García, C., Alonso, D., & Bellini, E. 2019, JCAP, 2019, 043
Gautier, T. N. I., Boulanger, F., Perault, M., & Puget, J. L. 1992, AJ, 103, 1313
Hajian, A., Viero, M. P., Addison, G., et al. 2012, ApJ, 744, 40
Halal, G., Clark, S. E., Cukierman, A., Beck, D., & Kuo, C. L. 2023, arXiv:2306.10107
Harris, C. R., Millman, K. J., van der Walt, S. J., et al. 2020, Natur, 585, 357
Henderson, S. W., Allison, R., Austermann, J., et al. 2016, JLTP, 184, 772
Hensley, B. S., Draine, B. T., & Meisner, A. M. 2016, ApJ, 827, 45
Hensley, B. S., Murray, C. E., & Dodici, M. 2022, ApJ, 929, 23
Hervías-Caimapo, C., Bonaldi, A., & Brown, M. L. 2016, MNRAS, 462, 2063
Hervías-Caimapo, C., & Huffenberger, K. M. 2022, ApJ, 928, 65
Hivon, E., Gorski, K. M., Netterfield, C. B., et al. 2002, ApJ, 567, 2
Huffenberger, K. M., Rotti, A., & Collins, D. C. 2020, ApJ, 899, 31
Hunter, J. D. 2007, CSE, 9, 90
Ingalls, J. G., Bania, T. M., Boulanger, F., et al. 2011, ApJ, 743, 174
Jarrett, T. H., Cohen, M., Masci, F., et al. 2011, ApJ, 735, 112
Kalberla, P. M. W., & Haud, U. 2019, A&A, 627, A112
Kilerci, E., Hashimoto, T., Goto, T., et al. 2023, ApJS, 265, 45
Knox, L. 1995, PhRvD, 52, 4307
Li, Z., Naess, S., Aiola, S., et al. 2020, JCAP, 2020, 010
Lungu, M., Storer, E. R., Hasselfield, M., et al. 2022, JCAP, 2022, 044
Mainzer, A. K., Eisenhardt, P., Wright, E. L., et al. 2005, Proc. SPIE, 5899, 262
Malinen, J., Montier, L., Montillaud, J., et al. 2016, MNRAS, 460, 1934
Marchal, A., & Miville-Deschênes, M. A. 2021, ApJ, 908, 186
Marsden, D., Gralla, M., Marriage, T. A., et al. 2014, MNRAS, 439, 1556
Martin, P. G., Blagrave, K. P. M., Lockman, F. J., et al. 2015, ApJ, 809, 153
Martin, P. G., Miville-Deschênes, M. A., Roy, A., et al. 2010, A&A, 518, L105
Mattila, K., Lemke, D., Haikala, L. K., et al. 1996, A&A, 315, L353
Meisner, A. M., & Finkbeiner, D. P. 2014, ApJ, 781, 5
Miville-Deschênes, M. A., Duc, P. A., Marleau, F., et al. 2016, A&A, 593, A4
Miville-Deschênes, M. A., Joncas, G., Falgarone, E., & Boulanger, F. 2003a, A&A, 411, 109
Miville-Deschênes, M. A., Levrier, F., & Falgarone, E. 2003b, ApJ, 593, 831
Miville-Deschênes, M. A., & Lagache, G. 2005, ApJS, 157, 302
Miville-Deschênes, M. A., Lagache, G., Boulanger, F., & Puget, J. L. 2007, A&A, 469, 595
Naess, S., Aiola, S., Austermann, J. E., et al. 2020, JCAP, 2020, 046
Naess, S., & Louis, T. 2023, OJAp, 6, 21
Naess, S., Madhavacheril, M., & Hasselfield, M., 2021 Pixell: Rectangular Pixel Map Manipulation and Harmonic Analysis Library, Astrophysics Source Code Library, ascl:2102.003
Onaka, T., Yamamura, I., Tanabe, T., Roellig, T. L., & Yuen, L. 1996, PASJ, 48, L59
Pingel, N. M., Dempsey, J., McClure-Griffiths, N. M., et al. 2022, PASA, 39, e005
Planck Collaboration I 2016, A&A, 594, A1
Planck Collaboration I 2020, A&A, 641, A1
Planck Collaboration III 2020, A&A, 641, A3
Planck Collaboration Int. LVII 2020, A&A, 643, 42
Planck Collaboration Int. XLVIII 2016, A&A, 596, A109
Planck Collaboration Int. XXIX 2016, A&A, 586, A132
Planck Collaboration Int. XXX 2016, A&A, 586, A133
Planck Collaboration Int. XXXII 2016, A&A, 586, A135
Planck Collaboration Int. XXXV 2016, A&A, 586, A138
Planck Collaboration Int. XXXVIII 2016, A&A, 586, A141
Planck Collaboration XI 2020, A&A, 641, A11
Planck Collaboration XXVIII 2016, A&A, 594, A28
Planck Collaboration XXX 2014, A&A, 571, A30
Seifried, D., Walch, S., Weis, M., et al. 2020, MNRAS, 497, 4196
Smith, K. M., Zahn, O., & Doré, O. 2007, PhRvD, 76, 043510
Stein, G., Alvarez, M. A., Bond, J. R., van Engelen, A., & Battaglia, N. 2020, JCAP, 2020, 012
Stinebring, D. R., Chatterjee, S., Clark, S. E., et al. 2019, BAAS, 51, 492
Thorne, B., Dunkley, J., Alonso, D., & Næss, S. 2017, MNRAS, 469, 2821
Thornton, R. J., Ade, P. A. R., Aiola, S., et al. 2016, ApJS, 227, 21
Tielens, A. G. G. M. 2008, ARA&A, 46, 289
Tokunaga, A. T., & Vacca, W. D. 2005, PASP, 117, 421
Vacher, L., Chluba, J., Aumont, J., Rotti, A., & Montier, L. 2023, A&A, 669, A5
van der Walt, S., Colbert, S. C., & Varoquaux, G. 2011, CSE, 13, 22
Viero, M. P., Wang, L., Zemcov, M., et al. 2013, ApJ, 772, 77
Virtanen, P., Gommers, R., Oliphant, T. E., et al. 2020, NatMe, 17, 261
Witstok, J., Shivaei, I., Smit, R., et al. 2023, Natur, 621, 267
Wright, E. L., Eisenhardt, P. R. M., Mainzer, A. K., et al. 2010, AJ, 140, 1868
Zaldarriaga, M. 2001, PhRvD, 64, 103001